ALLEVIATION OF DYNAMIC STALL INDUCED VIBRATIONS USING ACTIVELY CONTROLLED FLAPS

G. Depailler
Ph. D. Candidate
gdepaill@engin.umich.edu

Peretz P. Friedmann
François-Xavier Bagnoud Professor
peretzf@engin.umich.edu

Department of Aerospace Engineering, University of Michigan, Ann Arbor, Michigan

ABSTRACT

This paper presents a successful treatment of the helicopter vibration reduction problem at high advance ratios, taking into account the effects of dynamic stall. The ONERA model is used to describe the loads during stall, in conjunction with a rational function approximation for unsteady loads for attached flow. Single and dual actively controlled flaps are used to reduce vibrations. Successful vibration reduction is demonstrated over the entire range of advance ratios considered ($0.3 \leq \mu \leq 0.45$). This study represents the first successful implementation of vibration reduction in presence of dynamic stall, and physical explanation for the vibration reduction process is also provided. A methodology for accounting for the increased drag and power penalty associated with flap deflection is also described. Finally, saturation limits on the control deflections are imposed, which keep flap deflections in a practical range. Effective vibration reduction is achieved even when imposing practical saturation limits on the controller.

NOTATION

a, a_0, a_2	Separated flow empirical coefficients
b	Blade semi chord
C_{d0}	Blade drag coefficient in attached flow
C_L, C_M, C_D	Sectional lift, moment, drag coefficients
C_{D0}	Sectional drag coefficient when $C_L = 0$
c_b	Blade chord
c_{cs}	Flap chord
$C_{M_{Hz1}}$	Yawing moment coefficient about the hub
C_P	Helicopter power coefficient
c_{wu}	Multiplier for W_u weighting matrix
D	Drag force per unit span
$D_0,\ D_1$	Generalized flap motions
$\mathbf{d}$	Generalized force vector
e	Blade root offset from center of rotation
E, E_2	Separated flow empirical coefficients
f_1, f_2, f_3	Nondimensional semi-empirical functions
$F_{HX4}, F_{HY4}, F_{HZ4}$	Nondimensional 4/rev hub shears
h	Plunge displacement at the elastic axis
$\mathbf{h}$	Generalized motion vector
J	Objective function
J_R	Sum of the squares of the trim residuals
L	Lift force per unit span
L_b	Blade length
L_{cs}	Control surface length
M	Mach number
M_{AC}	Pitch moment per unit span
$M_{HX4}, M_{HY4}, M_{HZ4}$	Nondimensional 4/rev hub moments
N_b	Number of blades
p_0, p_1, p_c, p_h	Functions of M
r, r_0, r_2	Separated flow empirical coefficients
s_l	Function of M derived from flat plate theory
s_m, s_d	Empirical functions of M
t	Time

Presented at the American Helicopter Society 58th Annual Forum, Montréal, Canada, June 11-13, 2002.

t_0	Time when $\alpha = \alpha_{cr}$
$\mathbf{T}$	Transfer matrix
$\mathbf{u_i}$	amplitudes of control input harmonics
U	Air velocity relative to the blade section
U_P, U_T	Velocities perpendicular and tangential to flight direction experienced by blade, respectively
	value
$W_0,\ W_1$	Generalized airfoil motions
$\mathbf{W_z},\ \mathbf{W_u}$	Weighting matrices
x	Distance from blade root along undeformed elastic axis
x_{cs}	Control surface position
$X_{FA},\ Z_{FA}$	Longitudinal and vertical offsets between rotor hub and helicopter aerodynamic center
$X_{FC},\ Z_{FC}$	Longitudinal and vertical offsets between rotor hub and helicopter center of gravity
$\mathbf{z_i}$	amplitudes of vibratory load harmonics
α	Blade angle of attack
α_{cr}	Critical angle of attack for dynamic stall onset
α_f, α_s	Functions of M
α_R	Rotor shaft angle
γ	Lock number
Γ_1, Γ_2	Aerodynamic separated flow states
ΔC_L	Measure of stall
δ	Flap deflection, degrees
$\Delta C_{D0}, \Delta C_{d0}$	Increase in sectional drag coefficient and wing drag coefficient per unit span, respectively, for a flapped airfoil and wing.
Δt	Stall time delay
$\theta_0, \theta_{1s}, \theta_{1c}$	Collective and cyclic pitch angles
θ_t	Tail rotor constant pitch
κ_l	Function of M derived from flat plate theory
$\kappa_m, \kappa_d, \lambda$	Empirical functions of M
μ	Advance ratio
ρ	Air density
σ	Function of M
ϕ_R	Lateral roll angle
ψ	Azimuth angle
Ω	Rotor angular velocity
$\omega_{F1},\ \omega_{L1},\ \omega_{T1}$	Rotating fundamental blade frequencies in flap, lead-lag and torsion, respectively, nondimensionalized with respect to Ω.
$\dot{(\ )}$	Derivatives with respect to time

Subscripts

A	Attached flow
d	coefficient connected to drag
j	Represents l, m or d
l	coefficient connected to lift
m	coefficient connected to moment
S	Separated flow

Superscripts

1	Inboard flap (in dual flap configuration)
2	Outboard flap (in dual flap configuration)

INTRODUCTION AND BACKGROUND

One of the primary concerns in rotorcraft design is the issue of vibrations and its reduction. High levels of vibration may lead to passenger discomfort, fatigue of helicopter components and increased noise. These phenomena decrease rotorcraft performance and increase cost. Thus, the issues of vibration prediction and its reduction to the lowest possible levels are of primary importance to the helicopter designer.

The largest contributor to vibrations in a helicopter is the rotor. The rotor blades transfer vibratory loads from the hub to the fuselage at harmonics that are predominantly N_b/rev. The first methods devised for vibration reduction were passive, and were based on vibration absorbers and isolators. Later, active nethods have been implemented. In recent years, actively controlled trailing edge flaps have been investigated as a means for vibration control in helicopter rotors [1–5]. Experimental results from wind tunnels using the ACF were also presented by Straub [6]. Other vibration reduction studies using the ACF were also conducted [7, 8]. Additional information on vibration reduction using the ACF can be found in a recent survey paper [9].

Active control strategies have been developed that can reduce vibration levels well below those achieved through traditional passive methods such as dampers and mass tuning [1]. Among the active control approaches, two fundamentally different strategies have emerged:

higher harmonic control (HHC) and individual blade control (IBC). Three approaches have been used for individual blade control: actuation at the blade root [1], the actively controlled flap (ACF) [2–4], and active twist rotor blades [10, 11]. Vibrations are controlled at their source, on the rotor blades, by manipulating the unsteady aerodynamic loading in the rotating system.

Dynamic stall is a phenomenon that affects helicopter performance at high advance ratios, and the vibrations induced by dynamic stall limit helicopter performance at high speeds. A good description of the dynamic stall phenomenon is provided in Chapter 9 of [12]. The main effects of dynamic stall are : (1) a a hysteretic dynamic lift coefficient that is much higher than the corresponding static value, accompanied by (2) large pitching moments; and (3) large increases in the pitch-link vibratory loads that manifest themselves in the pilot's stick and negatively affect controllability. The specific problems of reducing vibrations due to dynamic stall has been studied by Nguyen [13] using HHC, and only a very small amount of vibration reduction was achieved.

Among the available models [12] of dynamic stall, two semi-empirical models have become quite popular and are often used for computational modeling of rotorcraft vibration. These are the ONERA model [14], later modified by Truong [15] and the Leishman-Beddoes model [16].

Recently, Myrtle and Friedmann [3] developed a new compressible unsteady aerodynamic model for the analysis of a rotor blade with actively controlled flaps. This model is based on rational function approximation (RFA) of aerodynamic loads, and it has been shown that it produces good accuracy in aeroelastic simulations. De Terlizzi and Friedmann [4] included a nonuniform inflow distribution calculation, based on a free-wake model, in the analysis, and simulated vibration reduction at high speeds as well as alleviation of blade vortex interaction (BVI) at low advance ratios.

Valuable experimental results on the practical implementation of the ACF and its application to vibration reduction in the open loop mode, on a Mach-scaled two bladed rotor, were obtained by Fulton and Ormiston [17]. These results were compared with the simulation described in Refs. 4 and 18 and the correlation with the experimental data was found to be quite good, in most cases.

Another problem encountered when using actively controlled flaps for vibration reduction is to account for the drag increase due to flap deflections. These flaps are intended to operate in an unsteady mode in the range of 2/rev–5/rev. There is no experimental data on increase in drag due to such time dependent flap deflections. Unfortunately even the steady data, that provides information on the static drag increase due to flap deflection, is scarce. Reliable computational tools, based on a computational fluid mechanics approach, are also not available. Since estimating the drag due to the flap deflection is an important consideration for the practical implementation of actively controlled flaps used for vibration reduction, one has no choice but use the static information available, and apply it in a quasistatic manner, to obtain an approximation to the increase in drag, and resulting power penalty associated with implementing the ACF concept for vibration reduction. The sources of information from which the drag increase due to a flap deflection can be estimated are listed below:

1. A semi-empirical method for correcting the drag on a generic wing/flap combination provided in a book by McCormick (Ref. 26).

2. Experimental data for a NACA 23012 airfoil with a $0.20c_b$ split flap presented in a report by Wenzinger and Harris [27]. This data was obtained on a 7 ft. wide airfoil, spanning the wind tunnel cross-section so as to simulate an infinite aspect ratio airfoil. This report also shows good correlation with an earlier report produced by the same authors [28].

3. Experimental information provided on a typical NACA 6-series profile with a $0.20c_b$ plain flap in Abbott and Von Doenhoff [29]. This data however is presented in a disorganized manner, which reduces one's confidence in using this data for incorporation in a rotor analysis code.

Based on this limited information a methodology for accounting for the flap increase due to flap deflections is developed.

This paper has several objectives: (1) Development of an improved rotor aerodynamic model by incorporating dynamic stall in the aeroelastic simulation of rotor vibratory loads in forward flight; (2) application of the simulation capability to the vibration reduction problem; and (3) development of a methodology for accounting for the increases in drag due to flap deflections that occur during vibration control and estimation of the power penalty associated with increased drag. This paper represents an important contribution toward the improved fundamental understanding of vibration modeling and its reduction using the ACF under dynamic stall conditions.

AEROELASTIC RESPONSE MODEL

Structural Dynamic Model

The structural dynamic model is directly taken from [2]. The rotor is assumed to be composed of four identical blades, connected to a fixed hub, and it is operating at a

constant angular velocity Ω. The hingeless blade is modeled by an elastic beam cantilevered at an offset e from the axis of rotation, as shown in Figure 1. The blade has fully coupled flap, lead-lag, and torsional dynamics. The strains within the blade are assumed to be small and the deflections to be moderate. The inertia loads are obtained from D'Alembert's principle and an ordering scheme is used to simplify the equations.

The control surfaces are assumed to be an integral part of the blade, attached at a number of spanwise stations. It is assumed that the control surfaces do not modify the structural properties of the blade, only the inertia and aerodynamic loads due to the flaps are accounted for. The control surface is constrained to pure rotation in the plane of the blade cross-section (see Fig. 1).

Aerodynamic Model

Aerodynamic Model For Attached Flow . Blade section aerodynamic loads are calculated using RFA, an approach described by Myrtle and Friedmann [3]. The RFA approach is an unsteady time-domain aerodynamic theory that accounts for compressibility, variations in the incoming flow and a combined blade, trailing edge flap configuration in the cross-section. These attributes make the RFA model particularly useful when studying vibration reduction in the presence of dynamic stall. The RFA approach generates approximate transfer functions between the generalized motion vector and the generalized attached flow force vector.

A non-uniform inflow distribution, obtained from a free wake model is employed. The free wake model has been extracted [18] from the rotorcraft analysis tool CAMRAD/JA [19]. The wake vorticity is created in the flow field as the blade rotates, and then convected with the local velocity of the fluid. The local velocity of the fluid consists of the free stream velocity, and the wake self-induced velocity. The wake geometry calculation proceeds as follows: (1) the position of the blade generating the wake element is calculated, this is the point at which the wake vorticity is created; (2) the undistorted wake geometry is computed as wake elements are convected downstream from the rotor by the free stream velocity; (3) distortion of wake due to the wake self-induced velocity is computed and added to the undistorted geometry, to obtain a free wake geometry. The wake calculation model [19] is based on a vortex-lattice approximation for the wake.

Aerodynamic Model For Separated Flow . Two families of semi-empirical models that are extensively used and reasonably well documented are available. These are the ONERA family of models and the Leishman-Beddoes model. Both are computationally efficient and thus are suitable for modeling aerodynamic responses in comprehensive rotor analyses.

Brief Comparison of the Two Dynamic Stall Models. A very comprehensive study that compares several dynamic stall models, in their ability to predict rotor behavior in presence of dynamic stall has been completed recently by a European study group [20]. Here we conduct only a brief comparison of the two models mentioned earlier. The Leishman-Beddoes lift model is slightly superior to the ONERA model, especially at peak lift, but the difference between the models is small elsewhere. The moment downward peak is also underpredicted by the ONERA model. However, the ONERA model is much more suitable for combination with the RFA type unsteady aerodynamic model which accounts for unsteadiness, compressibility and presence of flap. Furthermore, the ONERA model uses the same generalized motion vector $\mathbf{h} = [W_0, \quad W_1, \quad D_0, \quad D_1]$ for both regimes. In both RFA and the ONERA model, the attached flow transfer function is approximated by a rational transfer function. Both models are formulated in the time domain. Therefore, compatibility between attached flow and separated flow is not an issue.

The ONERA Models. In this paper, the ONERA model as modified and presented by Petot [14] is used. This model was modified by Truong, using the mathematical concept of a Hopf bifurcation [15, 21], but the resulting dynamic stall behavior displayed an oscillatory behavior which was not supported by experimental evidence. Useful modifications to the ONERA model were also introduced by Peters [22]. A brief description of the model as implemented in this paper is provided next. The airfoil velocity is expressed using the generalized motions W_0, W_1 shown in Fig. 2 and defined by:

$$W_0 = U\alpha + \dot{h}, \quad W_1 = b\dot{\alpha} \tag{1}$$

The model establishes a transfer function between the generalized motion vector $\mathbf{d} = [W_0, W_1, D_0, D_1]$ and the generalized force vector $\mathbf{h} = [L, M_{AC}, D]$. It is based on linear, time-varying coeffient differential equations. A first-order equation for attached flow

$$\begin{aligned} \dot{\Gamma_1} + \lambda\frac{U}{b}\Gamma_1 &= \lambda\frac{U}{b}p_0 W_0 + \lambda\frac{U}{b}W_1 + \alpha_s p_0 \dot{W}_0 \\ &\quad + \alpha_s \sigma \dot{W}_1, \end{aligned} \tag{2}$$

where $\lambda, \alpha_s, p_0, \sigma$ are functions of M derived from flat plate theory, and three second-order ones for separated flow:

$$\begin{aligned} \ddot{\Gamma_{j2}} + a_j.\frac{U}{b}\dot{\Gamma_{j2}} + r_j(\frac{U}{b})^2\Gamma_{j2} &= -[r_j(\frac{U}{b})^2 V\Delta C_L \\ &\quad + E_j.\frac{U}{b}\dot{W}_0, \end{aligned} \tag{3}$$

where $j = l, m, d$. The loads are derived from these ex-

pressions

$$L_S = \frac{1}{2}\rho c_b(s_l b\dot{W}_0 + \kappa_l b\dot{W}_1 + U(\Gamma_{l1} + \Gamma_{l2}) \quad (4)$$

$$M_{AC_S} = \frac{1}{2}\rho c_b^2(s_m b\dot{W}_0 + \kappa_m b\dot{W}_1 + U(\Gamma_{m1} + \Gamma_{m2}) \quad (5)$$

$$D_S = \frac{1}{2}\rho c_b(s_d b\dot{W}_0 + \kappa_d b\dot{W}_1 + U(\Gamma_{d1} + \Gamma_{d2}) \quad (6)$$

The attached flow loads in the ONERA model have been modified by Peters [22] to be consistent with Greenberg's unsteady aerodynamic theory. Other features of the ONERA dynamic stall model include the presence of a time delay for lift stall, expressed in non-dimensional time, and the presence of 18 empirical coefficients, 6 each $(r_{j0}, r_{j2}, a_{j0}, a_{j2}, E_{j2})$ associated with lift $(j = l)$, moment $(j = m)$, and drag $(j = d)$. The coefficients

$$r_j = (r_{j0} + r_{j2}.\Delta C_L^2)^2 \quad (7)$$

$$a_j = a_{j0} + a_{j2}.\Delta C_L^2 \quad (8)$$

$$E_j = E_{j2}.\Delta C_L^2 \quad (9)$$

The quantity ΔC_L is called a measure of stall and can attain two possible values:

$$\Delta C_L = 0 \quad (10)$$

$$\Delta C_L = (p_0 - p_1)(\alpha - \alpha_f)p_c[e^{p_h(\alpha-\alpha_{cr})} - 1] \quad (11)$$

The separation criterion is based on the angle of attack, and three possible cases can occur. Case 1: if $\alpha < \alpha_{cr} = 15^o(1 - M^2)$, ΔC_L is given by Eq. (10). Case 2: assume that at time $t = t_0$, $\alpha = \alpha_{cr}, \dot{\alpha} > 0$; then, at time $t > t_0 + \Delta t$, ΔC_L is given by Eq. (11). As ΔC_L is different from zero, separated flow loads become substantial. Case 3: when $\alpha < \alpha_{cr}$, ΔC_L is set to zero again (Eq. (10)) and the separated flow loads quickly decrease to zero. Attached and separated flow loads are then added at each blade section, i. e.:

$$C_L = C_{L_A} + C_{L_S}, \quad C_M = C_{M_A} + C_{M_S}, \quad C_D = C_{d0} + C_{D_S} \quad (12)$$

Combined Aerodynamic Model. The complete aerodynamic model used in this study consists of the RFA model for attached flow loads, using a free wake model in order to obtain the non-uniform inflow. The ONERA dynamic stall model is used for separated flow loads. Thus the complete aerodynamic state vector for each blade section consists of RFA attached flow states and ONERA separated flow states, together with the representation of the free wake.

DRAG CORRECTIONS FOR PARTIAL SPAN TRAILING EDGE FLAPS

In this section the information available for estimating drag increase due to flap deflection is summarized and used to develop an approximate methodology for introducing drag corrections.

Summary of the Methods Available

McCormick's Approach. A semi-empirical model for estimating the increment in profile drag coefficient due to the presence of a flap is described in a book written by McCormick [26] (p. 186). The model is not associated with any particular airfoil, and thus it is assumed to be suitable for generic airfoil flap configurations. The increase in wing profile drag coefficient per unit span [Eq. (6-22) page 186 of Ref. 26] is expressed as the product of three functions given below:

$$\Delta C_{d0} = f_1(\frac{c_{cs}}{c_b}) f_2(\delta) f_3(\frac{L_{cs}}{L_b}) \quad (13)$$

The following relations are provided for the functions. The function $f_1(\frac{c_{cs}}{c_b})$ is provided in graphical form in Ref. 26. The function $f_2(\delta)$ is given by:

$$f_2(\delta) = sin^2(\delta) \quad (14)$$

The function f_3 is taken to be

$$f_3 = \frac{L_{cs}}{L_b} \quad (15)$$

based on the recommendation made in Ref. 26. The figure in [26] yields:

$$f_1(\frac{c_{cs}}{c_b}) = f_1(0.20) = 1.0 \quad (16)$$

Therefore, Eq. (13) can be rewritten as:

$$\Delta C_{d0} = sin^2(\delta)\frac{L_{cs}}{L_b} \quad (17)$$

Note that Eq. (17) is independent of angle of attack or lift coefficient. Next, it is assumed that on the segments of the blade which have no flaps, the drag is not affected by the flap deflections; and on the portion where the flap is present the additional drag is uniformly distributed. Then, for the part $e \le x \le (x_{cs} - \frac{L_{cs}}{2})$ and $(x_{cs} + \frac{L_{cs}}{2}) \le x \le L_b$, $\Delta C_{D0} = 0$, and for the flapped part:

$$\Delta C_{d0} = \frac{1}{L_b}\int_{x_{cs}-\frac{L_{cs}}{2}}^{x_{cs}+\frac{L_{cs}}{2}} \Delta C_{D0} dx = \frac{L_{cs}}{L_b}\Delta C_{D0} \quad (18)$$

and:

$$\Delta C_{D0} = \frac{L_b}{L_{cs}} \Delta C_{d0} = \frac{L_b}{L_{cs}} \frac{L_{cs}}{L_b} \Delta C_{d0} = sin^2(\delta) \qquad (19)$$

Experimental Data for the Profile Drag Change due to Flap Deflections. Wenzinger and Harris [27] have presented experimental data for a NACA 23012 airfoil with a $0.20c_b$ split flap. This data was obtained using a 7ft. wide airfoil in a 7ft. wide wind tunnel, in order to simulate an infinite aspect-ratio wing so that induced drag is zero. It shows good correlation with an earlier study [28]. Data points have been reproduced on Fig. 3 as a function of angle of attack. For the NACA 23012 profile, when $\delta = 0^o$, the zero lift angle of attack is $\alpha = -1^o$. The measurements clearly show two characteristics of the profile drag curve: (a) a constant profile drag C_{D0} measured at $C_L = 0$; and (b) a component of the profile drag that is dependent on the airfoil lift coefficient. This data is provided because it forms the basis for the correction that will be developed to account for the flap drag increase due to flap deflections.

Correction for Unsteady Effects. The RFA model used in this study for lift and moment captures unsteady aerodynamic effects, but it does not address unsteady drag. The ONERA dynamic stall model [14] provides a description for unsteady drag in the dynamic stall region, but does not include unsteady drag effects in the unstalled region. However, the semi-empirical ONERA model does not include any effect due to the flap, and therefore, in the current study, static data for drag is used and applied in a quasi-static manner.

Comparison of Drag Models. Based on this concise summary of the aerodynamic information available, it is clear that the only useful information is the semi-empirical model represented by Eq. (19) augmented by the experimental data provided in Ref. 27. It is useful to compare the results obtained using Eq. (19) with the experimental data of Ref. 27.

The drag coefficient given by Ref. 27 and Eq. (19) when $\delta = 0^o$ is represented in Fig. 4. In this case, the correction for flap deflection, Eq. (19), is zero and McCormick's and Wenzinger and Harris' results coincide. The drag coefficient obtained by Wenzinger is compared to Eq. (19) for $\delta = 5^o$. Clearly, the semi-empirical correction provides only limited agreement with the experimental data of Ref. 27, the error is of the order of 20-30%. The profile used by Wenzinger and Harris is fairly close to airfoils used in rotorcraft, and therefore the curves in Ref. [27] are selected in this study as a basis for introducing drag corrections due to flap deflections.

Curve-Fitting of the Wenzinger-Harris Model. First consider curve fitting of C_{D0} as a function of flap deflections. Figure 5 shows C_{D0} as a function of δ. Due to a variety of practical considerations, the flap deflection will be limited to the range of $-10^o < \delta < 10^o$. For positive values of δ, $\delta > 0$, the experimental curve can be approximated by the straight line shown in Fig. 20:

$$C_{D0} = 0.01 + 0.001\delta \qquad (20)$$

According to Eq. (17), the effect of positive and negative flap deflections is identical. Therefore Eq. (20) is replaced by a more general form:

$$C_{D0} = 0.01 + 0.001|\delta| \qquad (21)$$

The influence of the lift coefficient C_L on drag C_D will not be considered in the attached flow region, where angles of attack are not too large, because it would prevent compatibility with the ONERA model at the onset of stall. The ONERA model is based upon a constant value for C_D and a variable value would involve a discontinuity in drag at dynamic stall onset.

Modification for Flap Chord. Note that in Refs. 27 and 29, the flap chord used was $0.20c_b$. In Eq. (13), f_1 depends on the flap chord, and the comparison conducted with Ref. 27 was based on $c_{cs} = 0.2c_b$ and $f_1 = 1.0$. In the aeroelastic response code $c_{cs} = 0.25c_b$ and the corresponding value of f_1 from Ref. 26 is $f_1 = 1.5$. This value of f_1 would produce drag coefficients that are unreasonably high. Therefore, the results of Ref. 27 will be modified for flap chord using the following approach:

1. For δ in degrees, Eq. (19) is approximated by:

$$\Delta C_{D0} = sin^2(\delta) \simeq \frac{\pi^2}{180^2}\delta^2 \qquad (22)$$

   The above equation means that ΔC_{D0} is approximately proportional to the square of δ.

2. For $c_{cs} = 0.25c_b$, the right-hand side of Eq. (22) is multiplied by $f_1 = 1.5$. Because the semi-empirical ΔC_{D0} is proportional to the square of δ in Eq. (22), while its experimental counterpart is a linear function of δ in Eq. (20), then the increase in the experimental drag coefficient must be multiplied by $\sqrt{1.5} = 1.225$ to account for the modification of flap chord to $c_{cs} = 0.25c_b$.

Thus, the model for drag due to the flap deflections at $c_{cs} = 0.25c_b$ combines elements of Refs. 26 and 27. It is given by the following relation:

$$C_{d0} = 0.01 + 0.001225|\delta| \qquad (23)$$

The Model Implemented in the Aeroelastic Response Code

In view of the above, the drag corrections for partial span trailing edge flaps used in the attached flow domain are:

$$C_d = 0.01 + 0.001225|\delta| \tag{24}$$

By contrast, the model used in [2] ("without correction") is:

$$C_d = 0.01 \tag{25}$$

In the baseline (uncontrolled) configuration, the flap is not deflected. In that case, the drag correction is zero.

METHOD OF SOLUTION

The blade is discretized [2] using the global Galerkin method, based upon the free vibration modes of the rotating blade. Three flapping modes, two lead-lag modes and two torsional modes are used in the actual implementation. The combined structural and aerodynamic equations form a system of coupled differential equations than can be cast in state variable form. They are then integrated in the time domain using the Adams-Bashfort DE/STEP predictor-corrector algorithm. The trim procedure [18] enforces three force equilibrium equations (longitudinal, vertical and lateral forces) and three moment equilibrium equations (roll, pitch and yaw moments). A simplified tail rotor model is used, using uniform inflow and blade element theory. The six trim variables are the rotor shaft angle α_R, the collective pitch θ_0, the cyclic pitch θ_{1s} and θ_{1c}, the tail rotor constant pitch θ_t and the lateral roll angle ϕ_R. The trim procedure is based on the minimization of the sum J_R of the squares of trim residuals. At high advance ratios ($0.30 < \mu \leq 0.35$) in the presence of dynamic stall, an autopilot procedure described in [23] is used to accelerate convergence to the trim state. At higher advance ratios ($0.35 < \mu$), an iterative optimization program based on Powell's method is used to find the trim variables that minimize J_R.

CONTROL ALGORITHM

This section presents a brief description of the control strategies that are employed in this aeroelastic simulation study of vibration reduction. Two different implementations of active control configurations are studied: (a) a single, actively controlled partial span trailing edge flap; and (b) a dual flap configuration, shown in Fig. 6, in which each flap is independently controlled. In each case, the controller will act to reduce the 4/rev vibratory hub shears and moments.

The control strategy is based on the minimization of a performance index described in [1–5, 24] that is a quadratic function of the vibration magnitudes $\mathbf{z}_i$ and control input amplitudes $\mathbf{u}_i$:

$$J = \mathbf{z}_i^T \mathbf{W_z} \mathbf{z}_i + \mathbf{u}_i^T \mathbf{W_u} \mathbf{u}_i, \tag{26}$$

The subscript i refers to the i-th control step, reflecting the discrete-time nature of the control. The time interval between each control step must be long enough to allow the system to return to the steady state so that the 4/rev vibratory magnitudes can be accurately measured. The matrices $\mathbf{W_z}$ and $\mathbf{W_u}$ are weighting matrices on the vibration magnitude and control input, respectively.

Conventional Control Approach (CCA)

A linear, quasistatic, frequency domain representation of the vibratory response to control inputs is used [2,3,18]. The input harmonics are related to the vibration magnitudes through a transfer matrix $\mathbf{T}$, given by

$$\mathbf{T} = \frac{\partial \mathbf{z_i}}{\partial \mathbf{u_i}}. \tag{27}$$

The optimal control is:

$$\mathbf{u}_i^* = -\mathbf{D}^{-1}\mathbf{T}^T\{\mathbf{W_z}\mathbf{z}_{i-1} - \mathbf{W_z}\mathbf{T}\mathbf{u}_{i-1}\}, \tag{28}$$

where

$$\mathbf{D} = \mathbf{T}^T\mathbf{W_z}\mathbf{T} + \mathbf{W_u} \tag{29}$$

Control in Presence of Flap Deflection Saturation

In the practical implementation of the ACF, adaptive materials based actuation, using piezoelectric or magnetostrictive materials, has been extensively studied. Adaptive materials are limited in their force and stroke producing capability, leading to fairly small angular deflections. From a control perspective this leads to saturation which introduces serious problems for vibration control. This important problem was studied and solved effectively in a recent paper by Cribbs and Friedmann [25]. This approach to dealing with saturation, described below, is also used in this paper. Saturation is treated by the auto weight approach [25]. The weighting matrix $\mathbf{W_u}$ is represented in a form which allows its modification by premultiplying it by a scalar c_{wu} that is continuously adjusted. The controller manipulates the scalar multiplier to provide the proper flap constraints. If the flap deflection is overconstrained, the controller reduces the value of c_{wu} and a new optimal control is calculated. If the flap deflection is underconstrained, the controller increases the value of c_{wu}

and a new optimal control is calculated. The iterative procedure reduces or increases c_{wu} until the optimal control converges to the desired deflection limits within a prescribed tolerance.

RESULTS

The helicopter configuration used in this study resembles approximately a MBB BO-105 four-bladed hingeless rotor. The data used in the computations is summarized in Table 1.The characteristics of the single and dual flap configurations are shown on Table 2.The portion of the blade spanned by the single flap is equal to the sum of the span covered by the dual flap configuration (see Fig. 6).

First, the effect of dynamic stall on the baseline 4/rev vibratory hub loads is considered. Figure 7 depicts the 4/rev vibratory loads at $\mu = 0.35$ when dynamic stall is included. All vibratory loads are increased significantly when dynamic stall is accounted for in the simulation. The pitching hub moment is increased by 50%, the rolling hub moment by 60%. The horizontal and lateral hub shears, as well as the yawing hub moment, are more than doubled. The most important vibratory component, the vertical hub shear, is increased by a factor of three. Therefore, the adverse effects of dynamic stall on vibratory hub loads are evident in the simulation.

Vibration reduction in the presence of dynamic stall, at high advance ratios, is considered next. For this case the vibration reduction capability of both single and dual flap configurations is considered. The vibration reduction capabilities of the two flap configurations are shown on Fig. 8. The single flap does not achieve reduction in vertical hub shear, but all other vibratory loads are reduced by 70-85%. The dual flap configuration reduces all loads by 70-95% and is at least 40% more effective than the single flap approach. This comparison shows the superiority of the dual flap configuration over the single flap. Excellent vibration reduction in presence of dynamic stall is achieved by this configuration. This reduction is much better than what has been documented in the literature before [13].

Figure 9 represents the baseline angle of attack distribution over the rotor disk, at $\mu = 0.30$. As expected, over the retreating blade, angles of attack become large and exceed α_{cr} between $\psi = 250^o$ and $\psi = 300^o$. Figure 10 represents the angle of attack distribution when optimal single flap control is applied. The presence of control reduces the angle of attack of the blade by approximately 1^o, over the whole surface of the rotor disk. This reduces the area affected by dynamic stall. Figure 11 depicts the dynamic stall locus, as defined by flow separation and reattachment, without control (diamonds) and with control (squares). The dynamic stall termination changes little in the presence of control (the difference in azimuth does not exceed 2^o), however the onset of dynamic stall has been significanlty altered. The boundaries of the dynamic stall zone is reduced by 30% from a region that extends between $240^o \leq \psi \leq 290^o$ to a region that is much narrower $255^o \leq \psi \leq 290^o$. This essentially explains the mechanism of vibration reduction by active control.

The optimal flap deflections required for the vibration reduction in the single flap configuration is shown on Fig. 12. The maximum flap amplitudes are about 15^o. Figure 13 displays the flap deflections for the dual flap configuration; here again, the maximum deflection of both flaps is about 15^o. However, actuator technologies based on smart materials severely limit flap deflections to a maximum of 5^o. Furthermore, flap deflections of 15^o are not acceptable from a practical implementation point of view. Therefore, additional results taking into account actuator saturation that allows practical limits on flap deflections have been obtained. The maximum allowable flap deflection for the cases considered here was set to 4^o, which is the value considered in an earlier study [25]. Results for vibration reduction are presented in Fig. 14 for the single flap configuration. The vertical hub shear is unchanged, but vibratory hub shear reduction is not affected by saturation; reductions of 70-80% are obtained again. However, vibratory hub moments are reduced 60-85% instead of 80-90%.

These results indicate that vibration reduction with the single flap configuration operating with and without saturation limits is similar, where the unsaturated flap reduces vibratory hub loads 10-30% more than the saturated flaps. These results are consistent with the observation made in an earlier paper [25] where the effects of dynamic stall were not included.

The flap deflections with and without saturation for the single flap configuration are shown on Fig. 15. The maximum allowed flap deflections occurs at $\psi = 225^o$, that is just before a large portion of the blade enters dynamic stall. This result confirms that the main feature of the control is to postpone dynamic stall entry (Figs. 9-10). When saturation is not taken into account, flap deflections are unconstrained, and large deflections can occur while producing only a small amount of vibration alleviation. This appears to be the case on the advancing portion part of the rotor disk. Figure 16 shows flap deflections for the inboard flap of the dual flap configuration. On the inboard flap, the saturation limit is never attained and the maximum flap deflection is less than 2^o. This is a reflection upon the nonlinearity in the problem combined with the existence of multiple minima in the objective function J. The outboard flap deflections are displayed in Fig. 17. Again the maximum flap deflection is not attained. For both the inboard and outboard flaps,

high amplitudes are evident, when saturation is included, in the range $180^o < \psi < 270^o$, which corresponds to the onset of dynamic stall. This is consistent with our earlier remark that control tends to delay the onset of dynamic stall.

The vibration reduction results presented in the previous figures were at an advance ratio of $\mu = 0.35$. However, it is well known that the unfavorable effects associated with dynamic stall increase rapidly with the advance ratio. This provides the justification for re-examining the results at a higher advance ratio, so as to identify possible problems that can emerge for these more severe flight conditions.

Vibration reduction results at the advance ratio $\mu = 0.45$ using the single flap configuration are presented in Fig. 18. Using the CCA approach, the vibration reduction achieved is 20-25% in longitudinal hub shear and yawing hub moment; 50% in lateral hub shear and rolling hub moment, 80% in pitching hub moment, however the vertical hub shear in increased by 80%, which is unacceptable since it represents the most important component of the vibrations. When saturation is accounted for, all loads decrease, between 10% for longitudinal force and 60% for vertical force. Therefore, vibration reduction is satisfactory, when actuator saturation is considered. This interesting result could be due to large nonlinearities associated with dynamic stall which give rise to multiple minima of J. Only under these extreme flight conditions are controlled vibratory loads higher than their uncontrolled level at $\mu = 0.30$.

Next, the influence of drag corrections for partial span trailing edge flap are considered. There is no need to trim the rotor again in order to incorporate the new drag due to flap deflections, because in the baseline configuration, $\delta = 0$ and thus drag is not altered. All simulations presented below feature dynamic stall. The effect of the drag coefficient on the effectiveness of the ACF as a vibration control device will be studied first. Figure 19 represents the baseline and controlled vibratory loads at $\mu = 0.35$, using a saturated single flap. No large vibratory load alteration is obvious when the drag modifications are implemented, although all of the vibratory hub shears and moments are 0%-15% higher. Nevertheless, a comparison with baseline vibratory loads shows that the new, modified drag model does not seem to jeopardize the effectiveness of the actively controlled flap as a vibration control device. Figure 20 depicts the flap deflections in both cases, for a single saturated flap. The drag corrections result in no appreciable flap deflection change. The nondimensional power needed to actuate the flap is shown on FIg. 21. The drag corrections bring little flap actuation power penalty.

Figure 22 represents the controlled optimal vibratory loads at $\mu = 0.35$, using an unsaturated single flap. Four of the vibratory loads are higher when the drag corrections are implemented. The two others, including the vibratory hub shear, are reduced by around 20%. Nevertheless, comparison with the baseline loads shows that the ACF is an effective vibration alleviation device. Figure 23 depicts the flap deflections in both cases, for a single unsaturated flap. Flap deflections obtained with and without drag corrections are not as similar as in the saturated flap case. Furthermore, the maximum flap deflection is reduced by around 10%, and flap deflections are usually lower when the drag corrections are implemented. This may be a consequence of the higher penalty associated with drag at high flap deflections (Eq. (24)). The nondimensional power needed to actuate the flap is represented on Fig. 24. When drag corrections are present, this power is significantly lower than in the uncorrected case; one of the power peaks disappeared while the others have a lower value. This may be due to the lower flap deflections and the lower rate of change of flap deflections. Furthermore, there is a small delay between the peaks. In all cases, the power needed to actuate the flap is less than a hundredth of a percent of the rotor power.

Next, the effect of the drag corrections on the rotor power is studied. Figure 25 represents the helicopter power coefficient in the baseline configuration (no control) and in the controlled configuration when both drag models are implemented. The helicopter power is defined as the power required to maintain a constant blade angular velocity ([2], Eq. (7.18)):

$$C_P = \frac{\Omega}{2\pi} \int_0^{2\pi} -C_{M_{Hz1}}(\psi) d\psi \tag{30}$$

In the saturated flap case, a comparison with the baseline helicopter power coefficient highlights a 2.5% rotor power change when the drag corrections are not present and a 3.5% change when they are present. Therefore, the increase in rotor power due to flap deflections is 34% higher when the drag corrections are implemented. In the unsaturated flap case, the rotor power increase is 3.5% without drag corrections, and 6% in with drag corrections. In that case, the drag corrections influence significantly the rotor power penalty due to the actively controlled flap.

CONCLUSIONS

A fairly extensive numerical simulation of vibration reduction at high speed flight using actively controlled flaps has been conducted. The ONERA dynamic stall model was used for the representation of the unsteady aerodynamic loading in the separated flow region. Both single flap and dual flap configurations were studied, and limits

on flap deflections were imposed. The principal conclusions obtained are provided below.

1. The ACF implemented either as a single flap or in the dual flap configuration is an effective means for alleviating the unfavorable effects due to dynamic stall.

2. The physical mechanism for reducing vibrations due to dynamic stall appears to be associated with delayed entry of the retreating blade into the stall region; combined with a reduction in the stall region over the area of the disk

3. The dual flap configuration appears to have an advantage over the single flap configuration in its ability to alleviate the undesirable effects associated with dynamic stall.

4. The actively controlled flap, implemented in either single or dual flap configurations, is more effective at alleviating dynamic stall effects than the HHC approach studied in Ref. 13. The primary reason for the effectiveness of ACF is due to the fact that it represents a local controller, that is inherently more suitable for dealing with local effects such as dynamic stall. The HHC approach affects the entire blade and thus is at a disadvantage when attempting to alleviate local effects.

5. Imposition of flap deflection limits, and the appropriate treatment of saturation play an important role in the ability of the ACF, in both configurations, to achieve alleviation of dynamic stall related effects. Therefore, a careful treatment of these issues is necessary for the practical implementation of the ACF in rotorcraft.

6. A methodology for drag rise due to flap deflection has been developed by using a combination of available experimental data and a semi-empirical approach. These drag corrections have been incorporated in the aeroelastic simulation code. The effectiveness of the ACF as a vibration reduction device is only slightly diminished as a result of this effect.

7. The power penalty associated with the ACF has been evaluated with and without drag corrections due to the ACF. When flap deflection saturation is implemented, this penalty is around 40% lower than in the unsaturated case, while vibration reduction is slightly inferior.

ACKNOWLEDGMENT

Partial support from the FXB Center for Rotary and Fixed Wing Air Vehicle Design for this research is gratefully acknowledged.

REFERENCES

[1] Friedmann, P. P. and Millot, T. A., "Vibration Reduction in Rotorcraft Using Active Control: A Comparison of Various Approaches," *Journal of Guidance, Control, and Dynamics*, Vol. 18, No. 4, 1995, pp. 664–673.

[2] Millott, T. A. and Friedmann, P. P., "Vibration Reduction in Helicopter Rotors Using an Actively Controlled Partial Span Trailing Edge Flap Located on the Blade," NASA CR-4611, 1994.

[3] Myrtle, T. F. and Friedmann, P. P., "Application of a New Compressible Time Domain Aerodynamic Model to Vibration Reduction in Helicopters Using an Actively Controlled Flap," *Journal of the American Helicopter Society*, No. 1, 2001, pp. 32–43.

[4] de Terlizzi, M. and Friedmann, P. P., "Active Control of BVI Induced Vibrations Using a Refined Aerodynamic Model and Experimental Correlation," *55th Annual Forum of the American Helicopter Society*, Montréal, Canada, May 1999, pp. 599–618.

[5] Friedmann, P. P., de Terlizzi, M. and Myrtle, T. F., "New Developments in Vibration Reduction with Actively Controlled Trailing Edge Flaps," *Mathematical and Computer Modeling*, Vol. 33, 2001, pp. 1055–1083.

[6] Straub, F. K., "Active Flap Control for Vibration Reduction and Performance Improvement," *Proceedings of the 51st American Helicopter Society Forum*, Fort Worth, Tex., May 1995, pp. 381–392.

[7] Straub, F. K. and Charles, B. D., "Comprehensive Modeling of Rotors with Trailing Edge Flaps," *Proceedings of the 55th Forum of the American Helicopter Society*, Montréal, Canada, May 1999.

[8] Chopra, I., Milgram, J. and Straub, F. K., "Comprehensive Rotorcraft Aeroelastic Analysis with Trailing Edge Flap Model," *Proceedings of the 52th Forum of the American Helicopter Society*, Washington, D. C., June 1996, pp. 715–725.

[9] Friedmann, P. P., "Rotary-Wing Aeroelasticity - Current Status and Future Trends," *Proceedings of the 39th AIAA Aerospace Sciences Meeting and Exhibit*, AIAA Paper No. 2001-0427, Reno, Nev., January 2001.

[10] Shin, S. J. and Cesnik, C. E. S., "Forward Flight Response of the Active Twist Rotor for Helicopter Vibration Reduction," *Proceedings of the 42th AIAA/ASME/ASCE/AHS/ACS Structures, Structural Dynamics and Materials Conference*, AIAA Paper No. 2001-1357, Seattle, Wash., April 2001.

[11] Wilbur, M. L., Mirick, P. H., Yeager, W. T., Langston, C. W., Shin, S. J., and Cesnik, C. E. S., "Vibratory Loads Reduction Testing of the NASA/Army/MIT Active Twist Rotor," *Proceedings of the American Helicopter Society 57th Annual Forum*, Washington, D. C., May 2001.

[12] Leishman, J. G., *Principles of Helicopter Aerodynamics*, Cambridge University Press, Cambridge, 2000.

[13] Nguyen, K., "Active Control of Helicopter Blade Stall," *AIAA Dynamics Specialists Conference*, AIAA Paper No. 96-1221, Salt Lake City, Utah, April 1996.

[14] Petot, D., "Differential Equation Modeling of Dynamic Stall," *La Recherche Aérospatiale*, Vol. 5, 1989, pp. 59–71.

[15] Truong, V. K., "2D Stall Model based on a Hopf Bifurcation," *Nineteenth European Rotorcraft Forum*, Paper No. C23, Cernobbio, Italy, September 1993.

[16] Leishman, J. G. and Beddoes, T. S., "A Semi-Empirical Model for Dynamic Stall," *Journal of the American Helicopter Society*, , No. 4, 1989, pp. 3–17.

[17] Fulton, M. and Ormiston, R. A., "Small-Scale Rotor Experiments with On-Blade Elevons to Reduce Blade Vibratory Loads in Forward Flight," *Proceedings of the 54th Annual Forum of the American Helicopter Society*, Washington, D. C., May 1998, pp. 433–451.

[18] de Terlizzi, M., *Blade Vortex Interaction and its Alleviation Using Passive and Active Control Approaches*, Ph.D. thesis, University of California, Los Angeles, 1999.

[19] Johnson, W., *A Comprehensive Analytical Model of Rotorcraft Aerodynamics and Dynamics, Vol. I: Theory Manual*, Johnson Aeronautics, Palo Alto, CA, 1988.

[20] Petot, D., Arnaud, G., Harrison, R., Stevens, J., Diederich, O., van der Wall, B. G., Young, C., and Széchényi, E., "Stall Effects and Blade Torsion - An Evaluation of Predictive Tools," *Journal of the American Helicopter Society*, Vol. 3, 1999, pp. 320–331.

[21] Truong, V. K., "Prediction of Helicopter Rotor Airloads Based on Physical Modeling of 3D Unsteady Aerodynamics," *Twenty-Second European Rotorcraft Forum*, Paper No. 96, Brighton, UK, September 1996.

[22] Peters, D. A., "Toward a Unified Lift Model for Use in Rotor Blade Stability Analyses," *Proceedings of the 40th Forum of the American Helicopter Society*, Arlington, Va., May 1984.

[23] Peters, D. A., Bayly, P. and Li, S., "A Hybrid Periodic-Shooting, Autopilot Method for Rotorcraft Trim Analysis," *Proceedings of the 52th Forum of the American Helicopter Society*, Washington, D.C., June 1996, pp. 780–792.

[24] Johnson, W., "Self-Tuning Regulators for Multicyclic Control of Helicopter Vibration," NASA TP-1996, 1982.

[25] Cribbs, R. and Friedmann, P. P., "Actuator Saturation and its Influence on Vibration Reduction by Actively Controlled Flaps," *Proceedings of the 42th AIAA/ASME/ASCE/AHS/ACS Structures, Structural Dynamics and Materials Conference*, AIAA Paper No. 2001-1467, Seattle, Wash., April 2001.

[26] McCormick, B. W., *Aerodynamics of V/STOL Flight*, Academic Press, New York, 1967.

[27] Wenzinger, C. J. and Harris, T. A., "Wind-Tunnel Investigation of a NACA 23012 Airfoil with Various Arrangements of Slotted Flaps," NACA Report 664, 1939.

[28] Jacobs, E. N. and Sherman, A., "Airfoil Section Characteristics as Affected by Variations of the Reynolds Number," NACA Report 586, 1937.

[29] Abbott, I. H. and von Doenhoff, A. E., *Theory of Wing Sections*, Mc Graw-Hill, New York, 1949.

Table 1: Elastic blade configuration

Rotor Data	
$N_b = 4$	$c_b = 0.05498 L_b$
$\omega_{F1} = 1.123$	$C_{do} = 0.01$
$\omega_{L1} = 0.732$	$C_{mo} = 0.0$
$\omega_{T1} = 3.17$	$a_o = 2\pi$
$\gamma = 5.5$	$\sigma = 0.07$
Helicopter Data	
$C_W = 0.00515$	
$X_{FA} = 0.0$	$Z_{FA} = 0.3$
$X_{FC} = 0.0$	$Z_{FC} = 0.3$

Table 2: Flap configurations

$c_{cs} = 0.25 c_b$	
Single Flap	
$x_{cs} = 0.75 L_b$	$L_{cs} = 0.12 L_b$
Dual Flap	
$x^1_{cs} = 0.72 L_b$	$L^1_{cs} = 0.06 L_b$
$x^2_{cs} = 0.92 L_b$	$L^2_{cs} = 0.06 L_b$

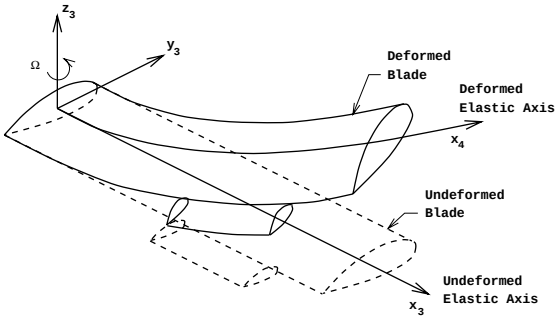

Figure 1: Schematic representation of the undeformed and deformed blade/actively controlled flap configurations.

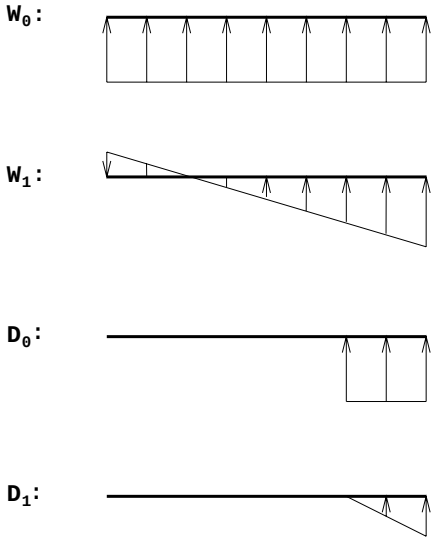

Figure 2: Normal velocity distributions corresponding to generalized airfoil and flap motions W_0, W_1, D_0, and D_1.

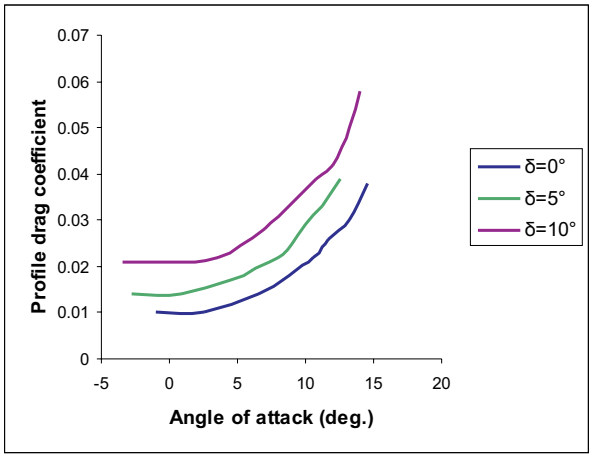

Figure 3: Eexperiments from Ref. 27, NACA 23012 airfoil, $c_{cs} = 0.2c$. The drag is plotted as a function of angle of attack.

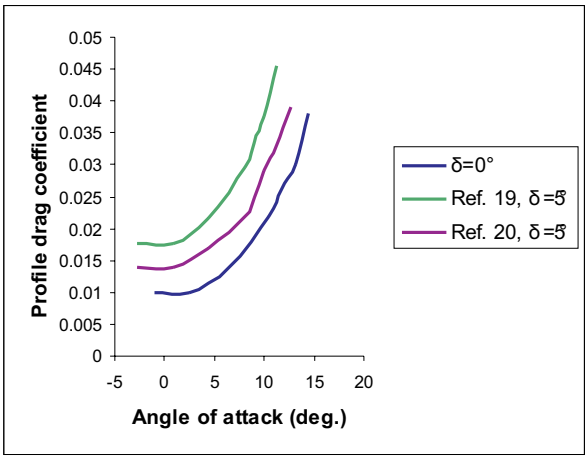

Figure 4: Comparison of drag models in Refs. 26 and 27. The drag is plotted as a function of angle of attack. Note: These models coincide for $\delta = 0^o$.

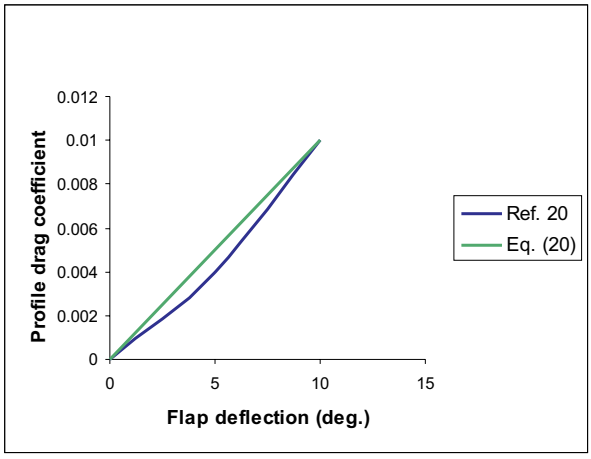

Figure 5: Model of the drag at zero lift.

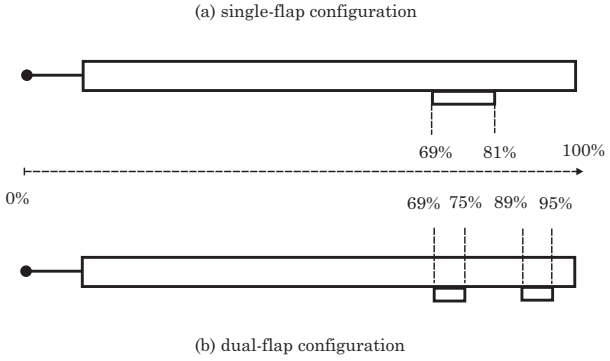

Figure 6: Single and dual flap configurations.

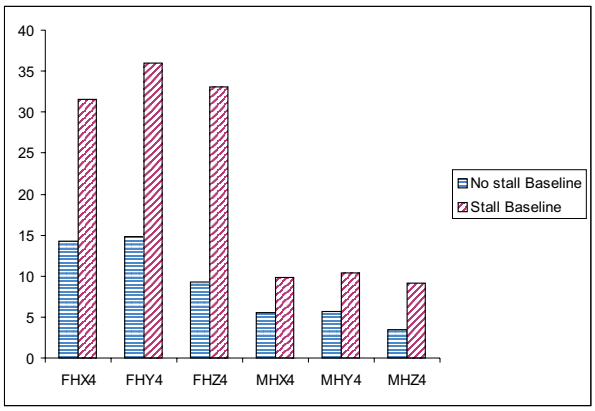

Figure 7: Influence of stall on baseline vibratory loads, μ=0.35.

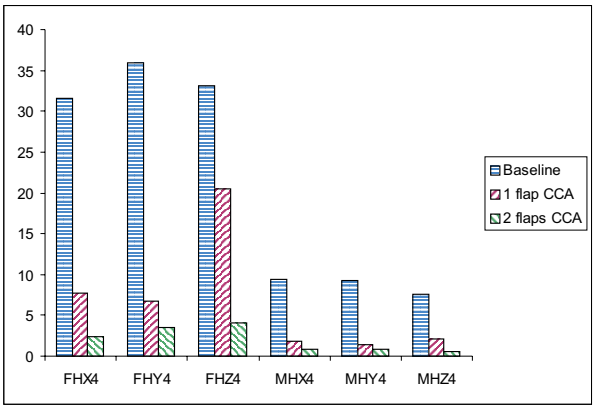

Figure 8: Vibration reduction, CCA, μ=0.35.

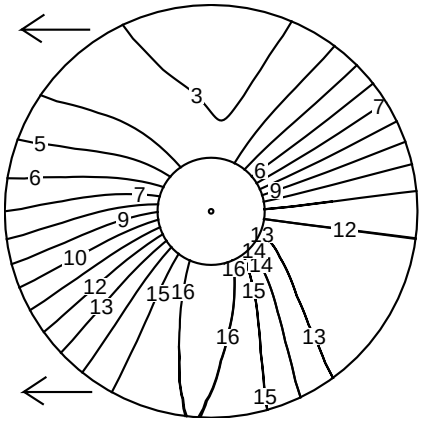

Figure 9: Angle of attack map in presence of dynamic stall, no control, μ=0.30. The center of the figure represents the hub region, the outer circle depicts the rotor disk and the arrows show the direction of forward flight. Aerodynamic loads are neglected in the inner circle.

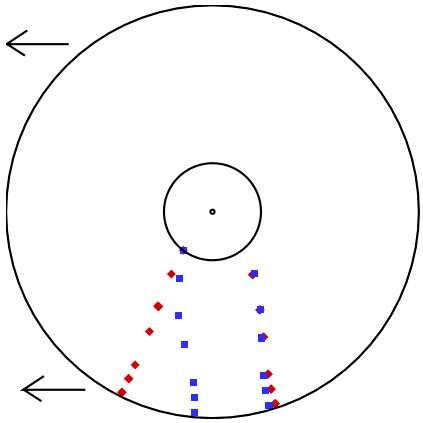

Figure 11: Dynamic stall locus control (squares) and no control (diamonds), μ=0.30. The center of the figure represents the hub region, the outer circle depicts the rotor disk and the arrows show the direction of forward flight. Aerodynamic loads are neglected in the inner circle.

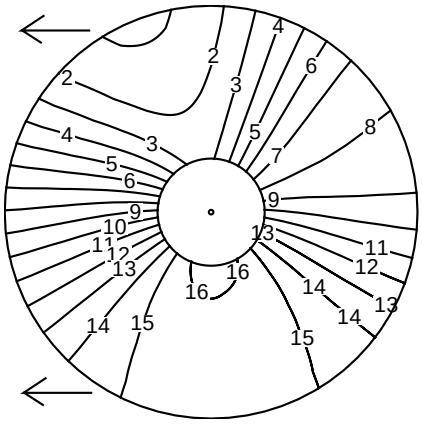

Figure 10: Angle of attack map in presence of dynamic stall, control, μ=0.30. The center of the figure represents the hub region, the outer circle depicts the rotor disk and the arrows show the direction of forward flight. Aerodynamic loads are neglected in the inner circle.

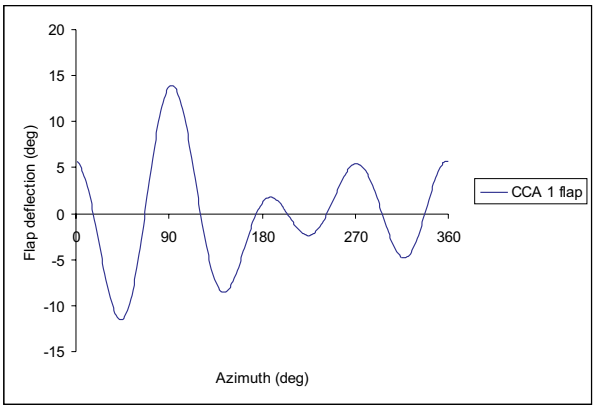

Figure 12: Flap deflections, CCA, single flap configuration, μ=0.35.

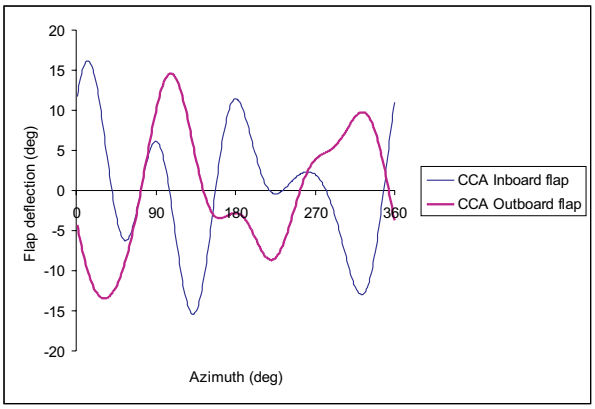

Figure 13: Flap deflections for dual flap configuration, CCA, μ=0.35.

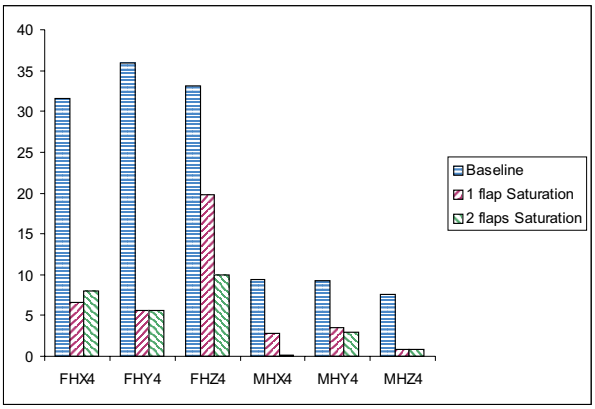

Figure 14: Vibration reduction with saturation limits, μ=0.35.

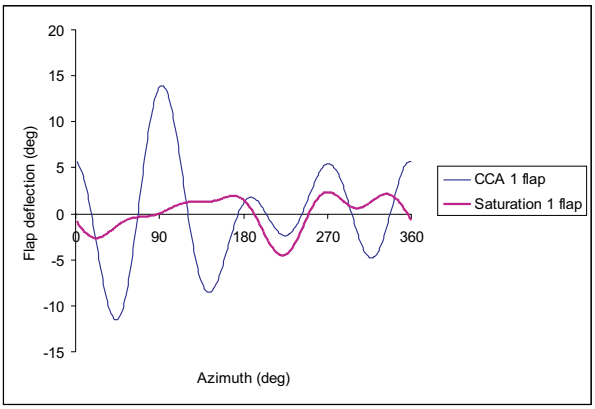

Figure 15: Flap deflections, effect of saturation, μ=0.35.

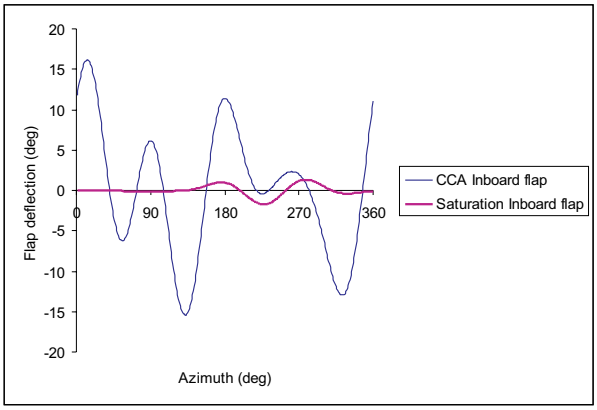

Figure 16: Inboard flap deflections, dual flap with saturation limits, μ=0.35.

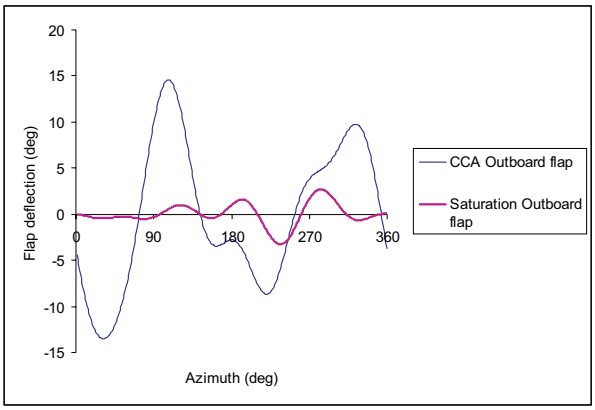

Figure 17: Outboard flap deflections, effect of saturation limits, μ=0.35.

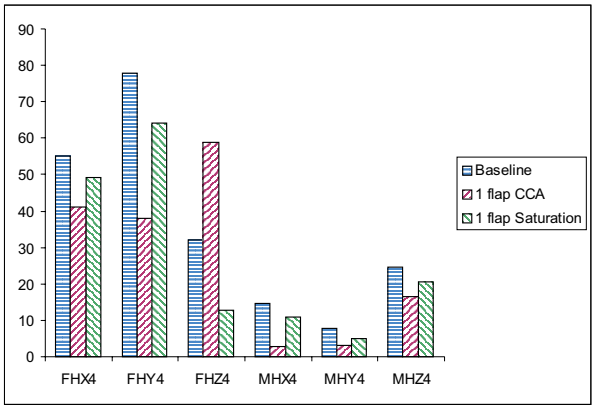

Figure 18: Vibration reduction, single flap, effect of saturation, μ=0.45.

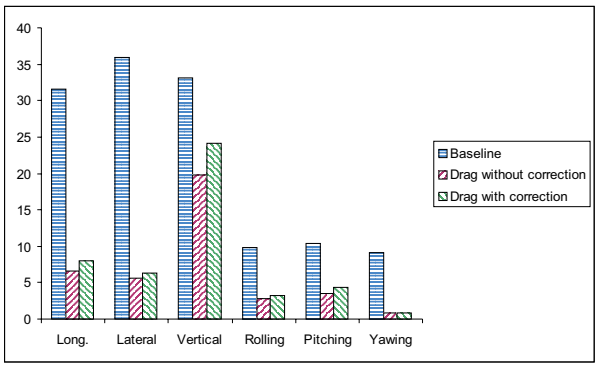

Figure 19: Vibration reduction at $\mu = 0.35$ in the single saturated flap configuration.

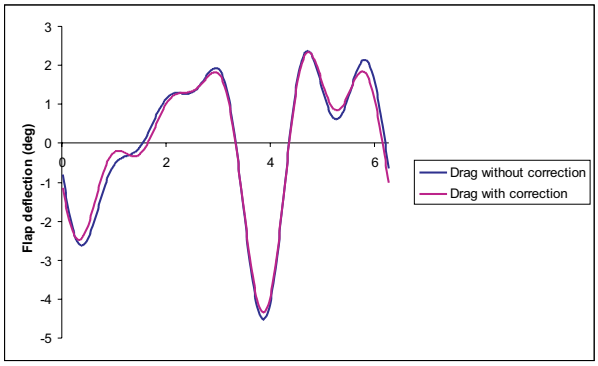

Figure 20: Flap deflections at $\mu = 0.35$ in the single saturated flap configuration.

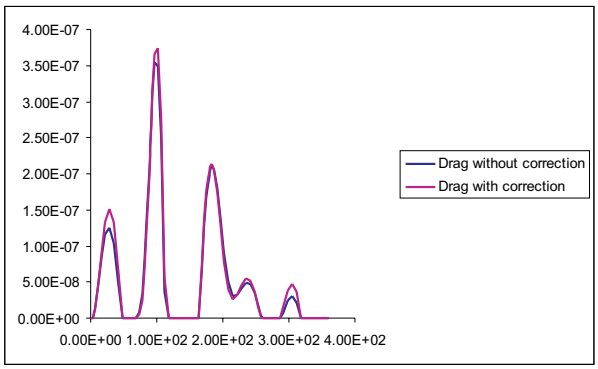

Figure 21: Nondimensional flap actuation power at $\mu = 0.35$ in the single saturated flap configuration.

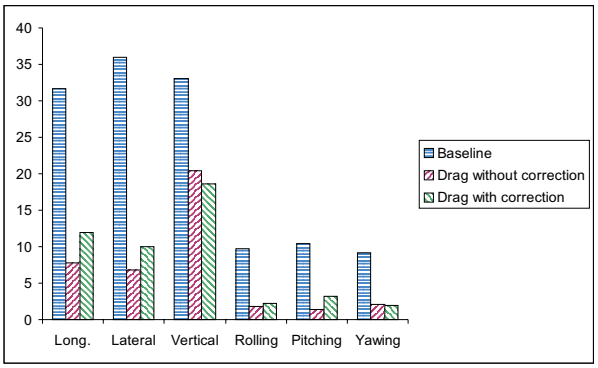

Figure 22: Vibration reduction at $\mu = 0.35$ in the single unsaturated flap configuration.

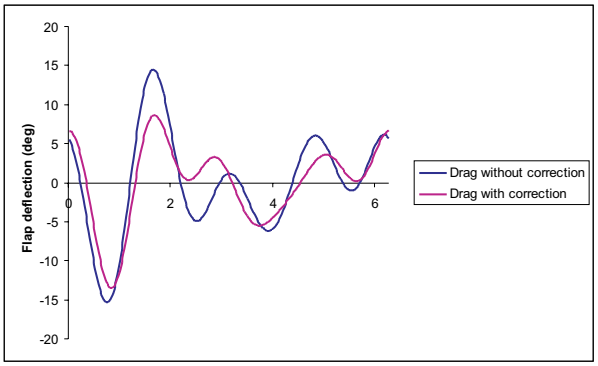

Figure 23: Flap deflections at $\mu = 0.35$ in the single unsaturated flap configuration.

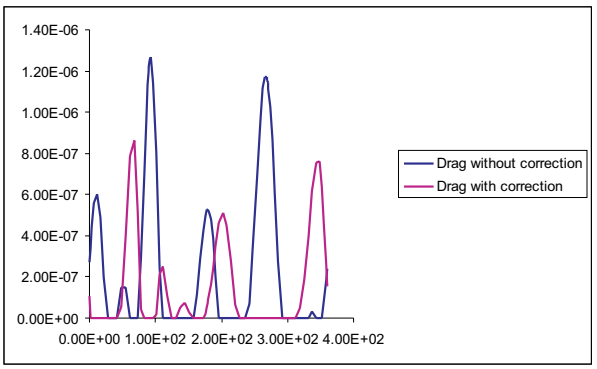

Figure 24: Nondimensional flap actuation power at $\mu = 0.35$ in the single unsaturated flap configuration.

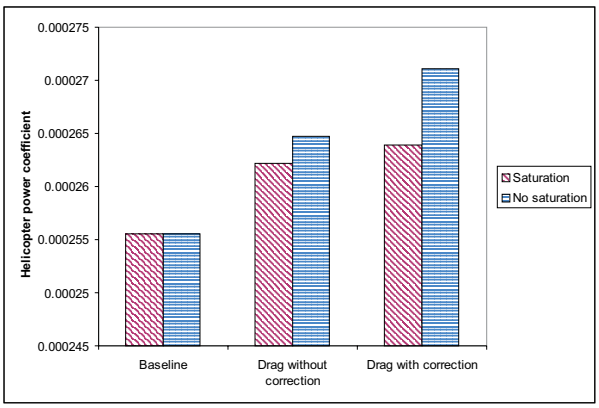

Figure 25: Rotor power at $\mu = 0.35$ in the single flap configuration.